

AKARI and Spinning Dust Emission

A look at microwave dust emission via the

Infrared

Aaron Christopher Bell

November 13, 2017

Abstract

The anomalous microwave emission (AME) still lacks a coherent explanation. Electric dipole emission by rapidly rotating dust (“spinning dust”) and magnetic dipole emission by grains with magnetic inclusions (“magnetic dust”) have emerged as potential explanations. We explore the scenario in which spinning polycyclic aromatic hydrocarbon molecules (PAHs) are the dominant carriers of the AME. We use data from the AKARI/Infrared Camera (IRC), due to its thorough PAH-band coverage, to compare AME (Planck Coll. astrophysical component separation product) with infrared dust emission. The results and discussion contained here apply to an angular scale of approximately 1° . In general, our results support an AME-from-dust hypothesis. At 1° angular resolution, we do not find evidence that the AME is exclusively carried by PAHs. The correlation of far IR dust emission with AME appears to be the best predictor, with MIR/PAH emission being marginally more weakly correlated with AME. In the case of λ Orionis, AME vs. PAH is at least as strong as AME vs. FIR. Higher resolution studies will be needed in the future to fully solve the AME mystery. We are consistent with previous studies in that the AME has a clear connection to interstellar dust, but a conclusive link to any particular population of dust is unapparent.

Contents

Abstract	i
1 Introduction	2
1.0.1 All-sky Astronomy	2
1.0.2 Infrared astronomy	3
1.1 Anomalous Microwave Foreground	4
1.1.1 Why microwave foregrounds are important	4
1.1.2 Discovery and first explorations	4
1.1.3 Proposed explanations	5
1.1.4 Spinning dust	6
1.1.5 Spinning PAHs?	7
1.1.6 Excitation factors	8
1.1.7 AME vs. IR in the literature	9
1.2 Scope of this Dissertation	10
1.2.1 An application of all-sky archival data	10
1.2.2 Testing the spinning PAH hypothesis	11
1.2.3 Limitations	11
1.2.4 Code availability	12

2	Data Sources	13
2.0.1	A collection of skies	13
2.0.2	Infrared Data	14
2.0.3	Planck COMMANDERAME Parameter Maps	18
2.0.4	All-sky Data Processing	23
3	All-sky Analysis	26
3.1	All-sky Pixel Domain Analysis	26
3.1.1	All-sky cross correlations	26
3.1.2	Pixel mask	27
3.1.3	AME data	27
3.2	Spatial variation of correlations	28
4	Analysis of an interesting AME region: λ Orionis	32
4.1	An interesting AME region	32
4.1.1	Where does the ring come from?	33
4.1.2	A well-studied region	33
4.2	Investigative approach	34
4.2.1	Data preparation	34
4.2.2	Extraction from HEALPix maps	35
4.2.3	Multi-wavelength characterization	35
4.2.4	Ionization fraction	35
4.2.5	SED Fitting	36
5	Discussion	40
5.1	AME:Dust	40

5.2	AME:PAH	42
5.3	AME: T, G_0	43
5.4	Microwave foreground component separation	43
6	Summary	44

List of Figures

2.1	Relative spectral response curves of the MIR bands used in this study, AKARI/IRC 9 μm , IRAS 12 μm , WISE 12 μm , AKARI 18 μm , and IRAS 25 μm . AKARI/IRC 9 μm , IRAS 12 μm , WISE 12 μm bands are dominated by PAH emission.	16
2.2	Ionization fraction of PAHs vs. band ratios of IRAS12 and 25, and WISE 12 and 25 μm bands vs. the AKARI 9 μm band, for three ISRF strengths: Top: $G_0 = 100$, Middle: $G_0 = 1000$, and Bottom: $G_0 = 10000$. These ratios are determined by assuming the SED template of Compiègne et al. (2011)	17
2.3	All-sky map of the ratio of two COMMANDER components- the frequency-varying AME component divided by the intensity of thermal dust emission at 545 GHz.	20
2.4	The peak frequencies of the varying component AME_{var} . The pink shaded region indicates frequencies not covered by either WMAP or Planck The green line at 33.5 GHz indicates the peak frequency of AME_{fix}	22
2.5	All-sky map of the peak frequencies of the varying component AME_{var} , corresponding to Fig. ??	23

2.6	Spdust template spinning dust profiles fitted by PC15 when calculating AME_{var} . The reference frequency, 22.8 GHz is indicated by the vertical green line. Each template has the same AME_{var} amplitude of 100 μ K, indicated by the horizontal green line, plotted to highlight the potential deviation between AME_{var} and the actual peak intensity.	24
3.1	ALL-SKY cross-correlation matrix for the 18 infrared bands sampled, and the AME map. The color-scale indicates (r_S). Results are based on the full sky (excluding pixels within 10° of the ecliptic plane).	28
3.2	ALL-SKY kernel density estimates of 12-band infrared photometry against the PR2 AME map. Pixels within 10° of the ecliptic plane are excluded. 'A' indicates AKARI; 'D', DIRBE; 'I', IRAS, and 'P' Planck. The number after each letter indicates the band central nominal wavelength in microns (or frequency in GHz, in the case of the Planck bands.)	29
3.3	Similar comparison to Fig. ??, with both the IR and the AME intensities scaled by the PR2 dust radiance (R) for each pixel. . .	30
3.4	Spatial map of r_s between the AME and IR intensity for 4 bands: 9 μm , 12 μm , 25 μm , and 140 μm . r_s is calculated for all NSIDE 256 pixels within each NSIDE 8 pixel-sized bin.	31

4.1	λ Orionis as it appears in the AKARI $9\ \mu\text{m}$ data. Contours indicate the AME, as given by the Planck PR2 AME map. The image is smoothed to a 1° PSF (much larger than the original 10 arc-sec map). The λ Orionis star itself is approximately located at the center of the image.	37
4.2	A grid of thumbnails showing the λ Orionis region's structure, at 12 wavelengths, along with AME contours (shown in white countours. Spatial correlation seems to be the best at the shortest and longest wavelengths (AKARI/IRC $9\ \mu\text{m}$ and Planck/HFI $550\ \mu\text{m}$). The images are smoothed and interpolated for demonstration. Figure ?? demonstrates the actual pixel grid used for the SED fitting and intensity correlation tests.	38
4.3	Pixel cross-correlation for all pixels in the λ Orionis cut-out region. r_s indicates the Spearman rank correlation coefficient for each plot.	39
1	Explained variance decline for principal component analysis performed on a set of 12 all-sky infrared maps. The first three components account for over 99% of the total variance. The PCA fit is performed on the whole sky, after whitening the data, using the "scikitlearn	48

Chapter 1

Introduction

“It is now plain that about 75% of the data we would like to have can be obtained from good ground-based sites”

-H. Johnson, 1966

1.0.1 All-sky Astronomy

All-sky astronomy is not new. Indeed, the notion of capturing a particular “object” or “source” with a camera and saving it for later investigation would be completely alien to the first astronomers and astronavigators. Absence of telescopes forced us to describe the sky in terms of its larger patterns, brightest characters. What is new however is the notion of preparing an archive of the sky itself for not only the research whims of a single investigator, team, institute, or even a single nation rather, all-sky surveys tend to be international endeavors in their production, and even more so in their utilization.

1.0.2 Infrared astronomy

Infrared astronomy was essentially non-existent as recently as the 1950s Johnson (1966) ¹. Compare this to visible wavelengths, a field so old we name it after the bio-evolutionary advent of sight, itself. Even radio astronomy with its own logistical and technological challenges, has been around since at least 1932.

Despite the title quote above, from (Johnson 1966), astronomers were apparently not content to be constrained by atmospheric IR windows, even from the best of ground-based sites. Or perhaps interests have shifted so dramatically since 1966, that all of the investigations enabled by rocket-based, space-based, even Boeing 747-based IR astronomy would have bored 75% of astronomers in the '60s. The meaning of “far infrared” has even redshifted, so to speak, from the Johnson (1966) definition of “4 to 22 μm ” ².

The ability to map and archive the sky with satellites - not only in the optical and infrared, but well into the microwave regime - has enabled interdisciplinary research of the ISM. Astrophysicists focused on the Milky Way itself are collaborating closely with those having more distant goals. ³

¹or 1920s, if we judge by the first IR observations

²For our purposes, we consider the FIR to cover 60 to 550 microns, partially out of convenience- FIR bands, in this paper, means the IRAS 60 and 100 micron, all four FIS bands, and the HFI 857 GHz and 545 GHz bands. The two IRC bands and the IRAS 12 and 25 micron bands we will refer to collectively as the MIR bands.

³Johnson (1966) did not offer a definition of “microwave”, though Penzias & Wilson (1965) had stumbled into microwave astronomy a year before.

1.1 Anomalous Microwave Foreground

1.1.1 Why microwave foregrounds are important

The study of our galaxy itself via microwave emission is surely worth chapters of discussion. The reason that galactic microwave emission has gotten the amount of attention it has in recent years however has little to do with galactic astronomy. Rather, the inconvenience our galaxy presents to extragalactic, cosmological astrophysics⁴ has brought the detailed decomposition of the microwave/radio regime of ISM to the forefront of Planck Collaboration paper titles.

The ISM has intruded into cosmological studies perhaps most prominently with the first claimed detection of B-mode polarization (Hanson et al. 2013; BICEP2 Collaboration et al. 2014; Flauger et al. 2014) and the subsequent counter-claim that this detection arose from galactic dust. More recently, Perrott et al. (2018) proposed that AMI-CL J0300+2613, a Sunyaev Zeldovich effect based galaxy cluster detection by AMI Consortium et al. (2012), may in fact be AME from a high galactic latitude dust cloud.

1.1.2 Discovery and first explorations

Since its first detection in early microwave observations, the anomalous microwave emission/foreground (AME) has been found to be a widespread feature of the microwave Milky Way (Dickinson et al. 2013). Kogut et al. (1996); de Oliveira-Costa et al. (1997); Leitch (1998) showed that the AME correlates very well with infrared emission from dust, via COBE/DIRBE and IRAS far-IR maps. However

⁴Indeed, without extragalactic research, there would be no need for the word “foreground” in describing galactic microwave emission.

there remains much mystery, except that the most likely source of the AME is interstellar dust (Ysard & Verstraete 2010; Tibbs et al. 2011; Hensley et al. 2016). Let alone uncertainty in the physical mechanism of the AME, and even assuming a dusty origin we are still puzzled as to the chemical composition and morphology of the carrier(s).

1.1.3 Proposed explanations

From the observed spatial correlation between AME and dust emerged two prevailing hypotheses:

1) Electric dipole emission by spinning small dust grains, a mechanism proposed in Erickson (1957) and Hoyle & Wickramasinghe (1970), with further discussion in Ferrara & Dettmar (1994). Draine & Lazarian (1998b) give the earliest thorough description, with substantial updates contributed more recently by Ysard & Verstraete (2010), Ali-Haïmoud et al. (2009), Hoang et al. (2010) and several others. Hensley & Draine (2017a) propose that such small spinning grains may consist primarily of silicates, and that this is allowed by observational upper-bounds of nanosilicate abundance, although nanosilicates have not yet been detected in the ISM. Dickinson et al. (2013) provide a detailed overview of AME and spinning dust literature.⁵

2) Magnetic dipole emission, caused by thermal fluctuations in grains with magnetic inclusions, proposed by Draine & Lazarian (1999). More recently, modeled spectra for potential candidate carriers have appeared in the literature: PAHs, grains with magnetic inclusions (Draine & Hensley 2013; Ali-Haïmoud 2014;

⁵An updated state of play of AME research has been submitted at the time of this writing (Dickinson, et al., submitted).

Hoang et al. 2016).

A third, but not widely accepted, possible explanation for AME is discussed in Jones (2009). They have suggested that the emissivity of dust, in the spectral range related to AME, could contain features caused by low temperature solid-state structural transitions.

1.1.4 Spinning dust

Spinning dust need not be the only emission mechanism, a convention as arisen in AME observational works. The photometric signature of the AME is frequently interpreted via spinning dust parameters (Ysard et al. 2011; Ali-Haïmoud 2010). Archival all-sky AME data products exclusively assume a spinning dust SED templates.⁶ Using the “spdust” spinning dust SED model code to fit excess microwave foreground emission has become as commonplace as fitting a modified blackbody function to the far IR.

We explore the case that the AME signature arises from spinning dust emission. If the AME is carried by spinning dust, the carrier should be small enough that it can be rotationally excited to frequencies in the range of 10-40 GHz, and must have a permanent electric dipole. Within contemporary dust SED models, only the polycyclic aromatic hydrocarbon family of molecules (PAHs), or nanoscale amorphous carbon dust fit these criteria. Those PAHs which have a permanent electric dipole (i.e. coranulene, but not symmetric molecules like coronene), can emit rotationally. However the carrier need not be carbon-based. Indeed, Hensley & Draine (2017a) claim that AME can be explained without car-

⁶Both WMAP and Planck used a base template with 30 GHz peak frequency, and an assumed cold neutral medium environment.

bonaceous carriers, using only spinning nanosilicates.

1.1.5 Spinning PAHs?

Assuming the rotational emission model of Draine & Lazarian (1998b), the AME signature (consistent with peaked, continuum emission having a peak between 15 and 50 GHz) implies very small oscillators (~ 10 nm).

In any case, the PAH class of molecules are the only spinning dust candidate so far which show both:

- 1) Evidence of abundance in the ISM at IR wavelengths, and
- 2) A predicted range of dipole moments (on order of 1 debye), to produce the observed AME signature (Draine & Lazarian 1998b; Lovas et al. 2005; Thorwirth et al. 2007). However, it should be noted that the current upper-bound on the abundance of nanosilicates, allows for a "spinning nanosilicate" explanation for the AME, as shown by Hensley & Draine (2017a). Due to the (apparently) continuous shape of the AME SED, a spinning dust explanation requires a distribution of dipole moments and/or rotational velocities of the carriers. Of course, the AME cannot simply be modeled by a distribution of carriers. Environmental factors affecting the rotational excitation of the carriers must be considered.

At the time of this writing, there is no strong argument in the literature that either PAHs or nanosilicates are physically preferred by AME observations. The physical plausibility of rapidly spinning PAHs and of rapidly spinning nanosilicates to produce the AME have both been outlined. This plausibility however is contingent on the abundance of PAHs or nanosilicates with appropriate dipole moments, and in regions with suitable excitation environments.

The arguments for or against particular carriers of the AME come from carrier abundance estimates and their statistical comparison with AME estimates. While neither nanosilicates nor any particular species of PAHs have been conclusively identified in the ISM, there is far more empirical evidence for PAH-like dust than there is for nanosilicates. Mid-infrared features associated with PAH-like aromatic materials have been observed. In fact, “the PAH features” are ubiquitous in the ISM (Giard et al. 1994; Onaka et al. 1996; Onaka 2000), such that the carriers must be abundant.⁷ There has yet to be any detection of features related to nanosilicates. There is only an upper-bound from IRTS observations of Onaka et al. (1996) and calculations by Li & Draine (2001). Hensley & Draine (2017a) argue that this upper-bound does not prohibit nanosilicates as the sole carriers of the AME.

1.1.6 Excitation factors

In the spinning dust model, there are several possible excitation factors for spinning dust. For the grains to have rotational velocities high enough to create the observed AME, they must be subject to strong excitation mechanisms. The dominant factors that would be giving grains their spin, are broken down by Draine (2011) into basically two categories: 1) Collisional excitation. 2) Radiative excitation, the sum of which could lead to sufficient rotational velocities for sufficiently small grains. However the extent of excitation will depend on environmental conditions, i.e. there will be more frequent encounters with ions and atoms in denser regions (so long as the density is not high enough to coagulate the small grains), and more excitation due to photon emission with increasing ISRF strength (Ali-

⁷Andrews et al. (2015) strongly argue for the existence of a dominant “grandPAH” class, containing 20 to 30 PAH species.

Haïmoud et al. 2009; Ali-Haïmoud 2014). One of the strongest potential excitation mechanisms listed in Draine (2011) is that of negatively charged grains interacting with ions. Thus not only must we consider environmental factors, grain composition and size, but also the ionization state of the carriers. (For example, ionized vs. neutral PAHs.) The dependence of the observed AME on ISM density is modeled by Ali-Haïmoud (2010), demonstrating that denser regions may have a stronger AME component (although it can be observationally challenging to resolve dense vs. diffuse AME producing regions.)

1.1.7 AME vs. IR in the literature

The overall pattern among large-scale studies seems to show that all of the dust-tracing photometric bands correlate with the AME (and each other) to first-order. On an all-sky, pixel-by-pixel basis, at 1° angular resolution, Ysard et al. (2010) find that $12\ \mu\text{m}$ emission, via IRAS, correlates slightly more strongly with AME (via WMAP) than with $100\ \mu\text{m}$ emission. They also find that scaling the IR intensity by the interstellar radiation field strength (given as G_0 , a measure of ISRF relative to that of the solar neighborhood) improves both correlations. They interpret this finding as evidence that AME is related to dust, and more closely related to the small stochastically emitting dust that is traced by $12\ \mu\text{m}$ emission.

However in a similar work, Hensley et al. (2016) report that the $12\ \mu\text{m}$ emission (via WISE) correlates less tightly with AME than with thermal dust radiance, using the Planck Collaboration dust and AME component-separation maps (Planck Collaboration et al. 2016a). Also at odds with Ysard et al. (2010), they report that AME correlates more strongly with $12\ \mu\text{m}$ intensity than with the in-

tensity scaled by the interstellar radiation field. They interpret this as AME and PAH emission both being correlated with the total dust radiance, but that there is no preferential relationship between PAHs and the AME.

The story is no more clear when looking at the average properties of individual regions. Planck Collaboration et al. (2014c) find that among 22 high-confidence "AME regions" (galactic clouds such as the ρ Ophiuchus cloud and the Perseus molecular cloud complex) AME vs. $12\ \mu\text{m}$ shows a marginally weaker correlation than AME vs. $100\ \mu\text{m}$ (via IRAS). Tibbs et al. (2011) examined the AME-prominent Perseus Molecular Cloud complex, finding that while there is no clear evidence of a PAH-AME correlation, they do find a slight correlation between AME and G_0 .

1.2 Scope of this Dissertation

1.2.1 An application of all-sky archival data

This is an astrophysical data archive based work. The primary goal is to highlight a particular application of multiwavelength (mid-IR to radio), cross-archive all-sky data analysis. We describe the interrelatedness between mid to far IR dust emission and possible microwave emission from dust. This is accomplished through an investigation of photometric all sky maps mainly from AKARI, IRAS, and Planck.

1.2.2 Testing the spinning PAH hypothesis

For the present work, we consider the spinning PAH hypothesis to have the highest degree of testability, due to the well-established presence of aromatic emission features in the ISM. We do not argue against the physical plausibility of nanosilicates to produce the AME. Indeed, there is no argument to date that these potential physicalities are mutually exclusive, as long as both potential carriers are sufficiently abundant.⁸

1.2.3 Limitations

We do not explore the modeling of microwave dust emission itself, rather the comparison of existing archival data and parameter maps. Modeling of the exact physical mechanism of the anomalous component of galactic microwave foreground emission from first principles is beyond the scope of this work. We consider this problem first on an all-sky basis, not focusing on any pre-selected object of the sky - in order to assess if there any general pattern between the IR and the AME, beyond the AME-dust correlation already described above. We then focus on a region highlighted by the Planck Collaboration as being especially worthy of further investigation (Planck Collaboration et al. 2016a), and has a resolvable topology even at 1-degree resolution. Essentially all of the analyses and conclusions presented in this work apply to an angular scale of approximately 1-degree, and only for the given component separation methods (Solar system, galactic, extragalactic) used by each of the data providers.

⁸Nor does spinning dust emission theoretically exclude magnetic dipole emission or microwave thermal dust emissivity fluctuations.

1.2.4 Code availability

This dissertation is accompanied by a github repository⁹ Virtually all of the analyses code are available in that repository, in the form of Jupyter notebooks (along with the figures and the code used to generate them.) The dust SED fitting code is not part of that repository, but is described in Galliano et al. (in prep.)

⁹Available at: <https://github.com/aaroncnb/CosmicDust>.

Chapter 2

Data Sources

2.0.1 A collection of skies

This work relies completely on all-sky surveys. All of the maps utilized are photometric-band infrared maps, except for the AME data, which is an all-sky component separation analysis product, from the Planck Collaboration’s efforts to separate galactic foregrounds from the CMB.

Primary band of interest

¹ The AKARI/IRC 9 μm band (A9) provides uniquely complete coverage of the PAH bands at 6.2, 7.7, 8.6, and 11.2 μm , and may be an excellent tool for testing PAH-related hypotheses on an all-sky basis. The combination of A9 with W12 and/or I12 may be especially insightful. In total, we employ all-sky maps from 12 photometric bands, spanning the wavelength range of 6.9 μm to 550 μm ²

¹Not to be confused with “The band primarily interested” in dust, Queen.

²Planck bands are named according to their central frequency, not wavelength.

Table 2.1: Observational data sources used in this article

Instrument	Central Wavelength	FWHM	Cali	Reference
AKARI/IRC	9 μm	$\sim 10''$	$< 10\%$	(Ishihara et al. 2010)
AKARI/IRC	18 μm	$\sim 10''$	$< 10\%$	"
AKARI/FIS	65 μm	63"	$< 10\%$	(Doi et al. 2015; Takita et al. 2015)
AKARI/FIS	90 μm	78"	$< 10\%$	"
AKARI/FIS	140 μm	88"	$< 10\%$	"
AKARI/FIS	160 μm	88"	$< 10\%$	"
IRAS/IRIS	12 μm	4.0'	$< 5.1\%$	(Miville-Deschênes & Lagache 2005)
IRAS/IRIS	25 μm	4.0'	$< 15.1\%$	"
IRAS/IRIS	60 μm	4.2'	$< 10.4\%$	"
IRAS/IRIS	100 μm	4.5'	$< 13.5\%$	"
Planck/HFI	345 μm	4.7'		(Planck Collaboration et al. 2014a)
Planck/HFI	550 μm	4.3'		"

2.0.2 Infrared Data

AKARI

The AKARI infrared space telescope revealed an entire sky of infrared light, from the mid to far infrared, via two instruments (Murakami et al. 2007) the Infrared Camera (IRC)(Onaka et al. 2007) and the Far Infrared Surveyor (FIS) (Kawada et al. 2007a).

AKARI/IRC PAH feature coverage The IRC's 9 μm band all-sky map demonstrates the abundance of the PAH bands carrier in the Milky Way (Ishihara et al. 2010). Figure ?? shows the coverage of the MIR bands along with an example galactic cirrus SED. The 9 μm band uniquely covers major ionized PAH features at 6.2 and 7.7 μm ; as well as neutral PAH features at 8.6 and 11.2 μm across the entire sky (Onaka et al. 2007). The IRAS 12 μm band covers the 11.2 and 8.6 μm features, and the similarly-shaped WISE 12 μm band covers primarily the

11.2 μm feature.

In-band contribution from PAHs According to this distribution of PAH features across the response filters, it is expected that the IRC 9 μm band is most dominated by PAH emission even with increasing G_0 . These contributions remain relatively constant out to a G_0 of about 100, with the contribution from warm dust becoming a larger factor for the IRAS 12 μm and WISE 12 μm bands. Thus, according to the DL01 template, IRC 9 μm should have the highest contribution from PAHs out to extreme radiation fields.

Potential to trace PAH ionization Fig. ?? demonstrates how the band ratios of the IRC 9 μm band vs. the other MIR bands change with different modeled PAH ionization fractions (determined using the DustEM default model template, by Compiègne et al. (2011)). This band ratio can be determined, because the IRC9 filter is more sensitive to ionized PAH features, relative to IRAS12 or to WISE12. IRC 9 μm shows a larger contribution from ionized PAHs, by about 16 percent, and a conversely smaller contribution from neutral PAHs.

We utilize the most recent version of the IRC data (Ishihara, et al., in prep.) This version has had an updated model of the Zodiacal light, fitted and subtracted. The details of the improved Zodi-model, which offers an improvement over that used for the IRAS all-sky maps, are given in Kondo et al. (2016).

The AKARI Far Infrared Surveyor (FIS) gives us photometric data around the peak of the typical thermal dust SED. FIS was equipped with four wavebands: two narrow bands centered at 65 μm and at 160 μm , and two wide bands at 90 μm and at 140 μm . An all-sky survey was carried out at each band (Kawada et al.

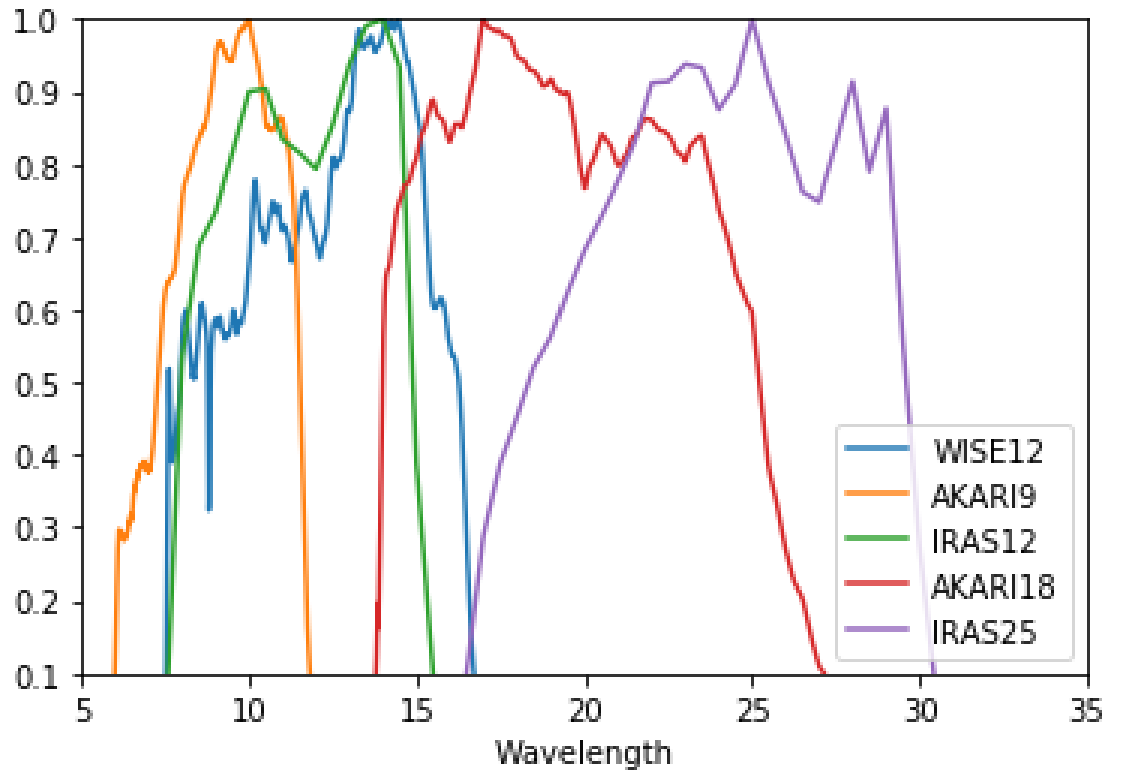


Figure 2.1: Relative spectral response curves of the MIR bands used in this study, AKARI/IRC 9 μm , IRAS 12 μm , WISE 12 μm , AKARI 18 μm , and IRAS 25 μm . AKARI/IRC 9 μm , IRAS 12 μm , WISE 12 μm bands are dominated by PAH emission.

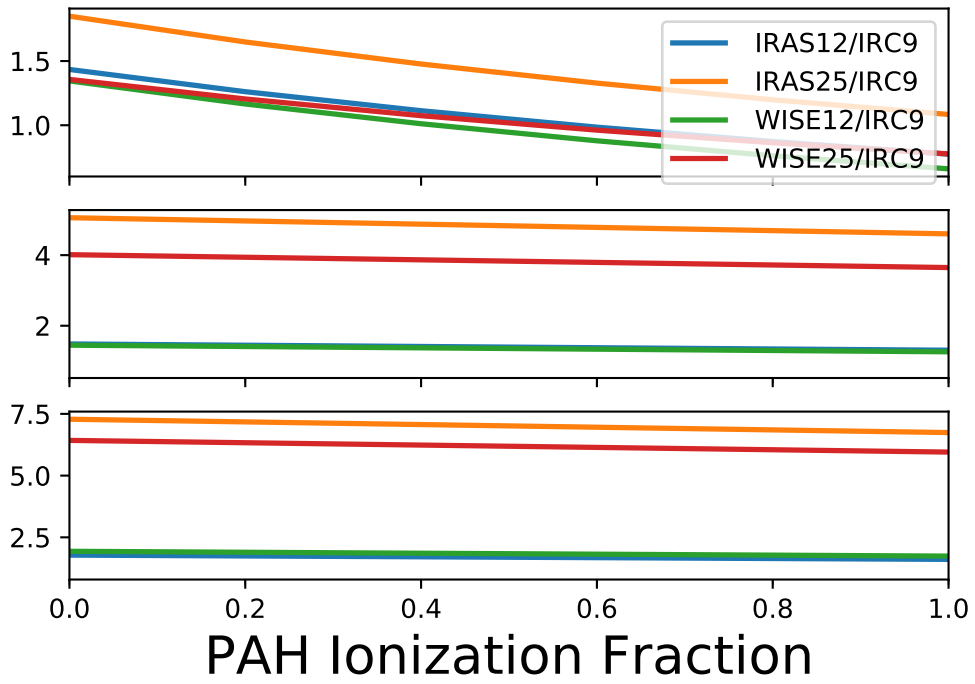


Figure 2.2: Ionization fraction of PAHs vs. band ratios of IRAS12 and 25, and WISE 12 and 25 μm bands vs. the AKARI 9 μm band, for three ISRF strengths: Top: $G_0 = 100$, Middle: $G_0 = 1000$, and Bottom: $G_0 = 10000$. These ratios are determined by assuming the SED template of Compiègne et al. (2011)

2007b), and the processed maps have been publicly released (Doi et al. 2015).

The Planck Space Observatory (Planck) High Frequency Instrument (HFI) all-sky maps, spanning 100 to 857 GHz (Planck Collaboration et al. 2014a) help constrain the far IR dust emissivity. This study utilizes the 857 GHz (345 μm) and 545 GHz (550 μm) bands.

Data from the Infrared Astronomical Satellite (Neugebauer et al. 1984) all-sky surveys are used to supplement the similarly-centered AKARI photometric bands. The IRAS 12 μm band is similar to the AKARI 9 μm band in terms of the sky coverage, central wavelength, and especially in that both surveys are heavily dominated by zodiacal light. We use the Improved Reprocessing of the IRAS Surveys (IRIS) (Miville-Deschênes & Lagache 2005), which use undergone a zodiacal-light removal. The Zodiacal light model, however differs between the two bands. The IRAS Zodi-subtraction is primarily based on the Kelsall et al. (1998) model.

2.0.3 Planck COMMANDERAME Parameter Maps

We utilize the COMMANDER-Ruler astrophysical component separation maps, from the Planck Collaboration’s Public Data Release 2 (hereafter, PR2). Details of the foreground contribution estimates are given in Planck Collaboration et al. (2014b). We first describe the ‘non-AME’ components, so as to not give any indication that their estimation is trivial.

Synchrotron

While the Planck observations themselves do limit our resolution when assessing the AME - it is in fact the primary constraint on synchrotron emission, 408 MHz map by Haslam et al. (1982) that is the major resolution limiting factor. While an impressive, pioneering effort for to reveal the low-frequency sky, (Haslam et al. 1982) is limited to an approximately 1 degree resolution. The map also contains many artifacts. For the time being however, it is still the most synchrotron-dominated all-sky map available, and for this reason PC15X included it in their COMMANDER component separation. The final synchrotron product produced by COMMANDER (hereafter, PCSync) highly resembles the (Haslam et al. 1982) map, however it is also demonstrated PCSync does not fully capture the synchrotron signal. This can be visualized by inspecting the PCAME:PCdust ratio map (see Fig. ??), which ? describe as containing synchrotron emission patterns at high latitudes.

Free-free emission

Unlike the PCSync component, the fitting of the Planck COMMANDER free-free component map (hereafter, PCff) does not employ any free-free dominated emisison map.³.

³The Planck AME paper, Planck Collaboration et al. (2014c), had employed the H- α map by Reynolds et al. (1998)

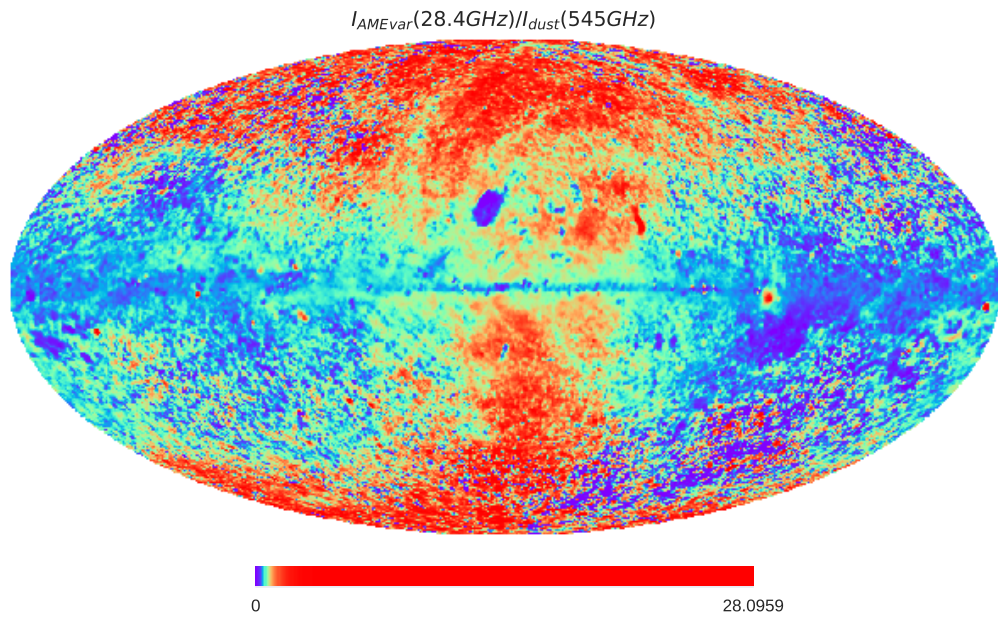


Figure 2.3: All-sky map of the ratio of two COMMANDER components- the frequency-varying AME component divided by the intensity of thermal dust emission at 545 GHz.

Thermal dust emission

COMMANDER-AME: Peak Frequency Distribution

$I_{AME}\nu_{var}$ The Planck-COMMANDER component separation products contain estimates of known microwave foreground components (free-free, synchrotron, thermal dust emission ⁴) contributions to the Planck photometric bands. In addition, there is an “AME component map”, which presumes that AME originates from spinning dust. While acknowledging that such a decomposition lacks a physical justification, Planck Collaboration et al. (2016a) break the AME into two components: a spatially varying peak frequency component, and a spatially constant peak frequency component. However as seen in Fig. ??, virtually all of the fitted peak frequencies for AME_{var} beyond the reach of WMAP and Planck. Only the fitted global frequency, 33.5 GHz for the spatially constant component, is covered.

The COMMANDER maps give each component’s intensity at a different “reference frequency” (corresponding to photometric bands). In other words, the COMMANDER AME intensities are not peak intensities. Moreover they are intensities calculated for a single template spinning dust spectrum- but one that has been log-log translated to fit the observations (a demonstration of such shifted templates, for a common “reference intensity” at a common “reference frequency”, is shown in Fig. ??). The physical parameters in the spinning dust model, “spdust” are not varied.

For these reasons, we are very cautious in deriving conclusions from comparisons with the COMMANDER AME map. Indeed, the authors themselves include

⁴“Thermal dust emission” in the COMMANDER context refers to dust emission in the Rayleigh Jeans-regime, as the COMMANDER fitting does not include photometric constraints on the thermal emission peak, or consider small grain emission on the Wiens side.

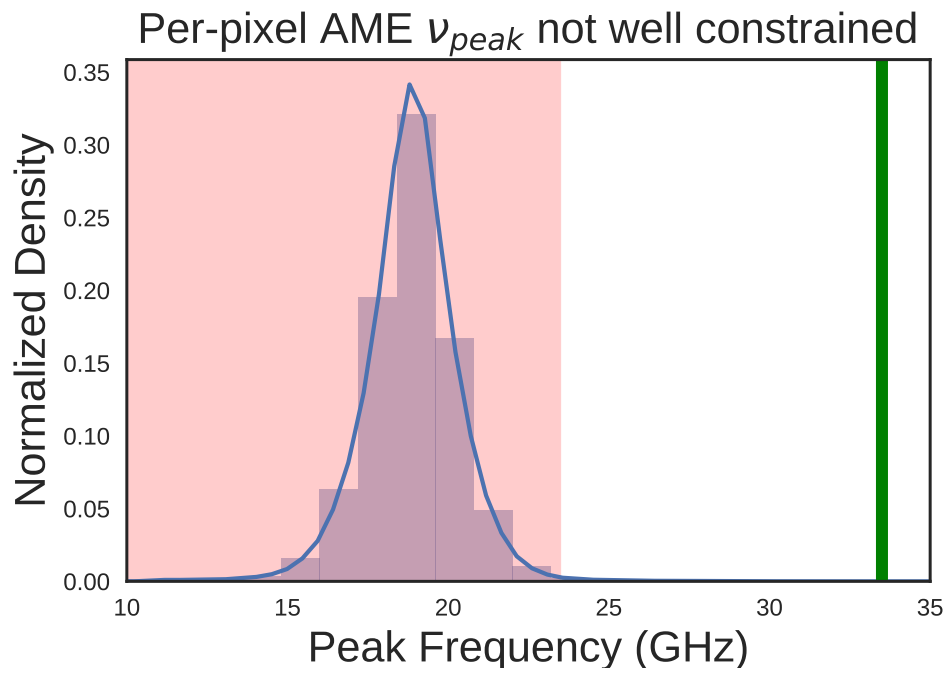


Figure 2.4: The peak frequencies of the varying component AME_{var} . The pink shaded region indicates frequencies not covered by either WMAP or Planck. The green line at 33.5 GHz indicates the peak frequency of AME_{fix} .

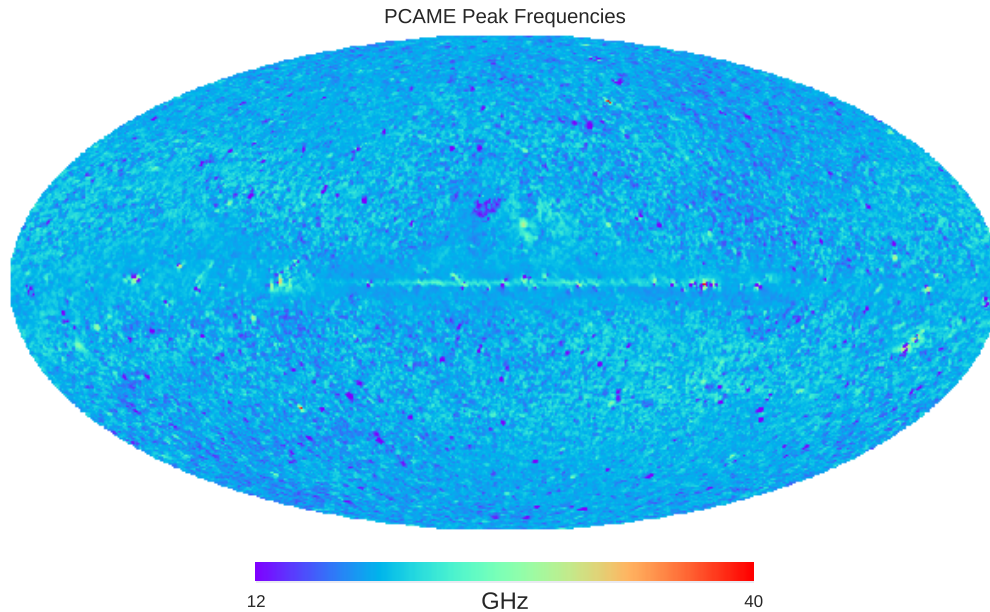


Figure 2.5: All-sky map of the peak frequencies of the varying component AME_{var} , corresponding to Fig. ??.

a similar disclaimer. However since there is currently no better all-sky component separation available⁵, and carrying out a spinning dust modeling and component separation is beyond the scope of this work, we proceed with care.

2.0.4 All-sky Data Processing

The HFI, FIS, and IRIS maps used here are downloaded from their respective online repositories, as all-sky HEALPix⁶ maps (Górski et al. 2005). NSIDE 2048 maps. In the case of the IRC maps, we first create HEALPix maps from the 4,857

⁵Indeed, improving on the COMMANDER AME map would be extremely difficult without lower frequency constraints and/or higher resolution observations of not only the AME itself but the contribution from synchrotron and free-free emission.

⁶HEALPix core software is described at <http://healpix.sourceforge.net>. The HEALPix python package “healpy” used in this work is available at: <https://github.com/healpy/healpy>

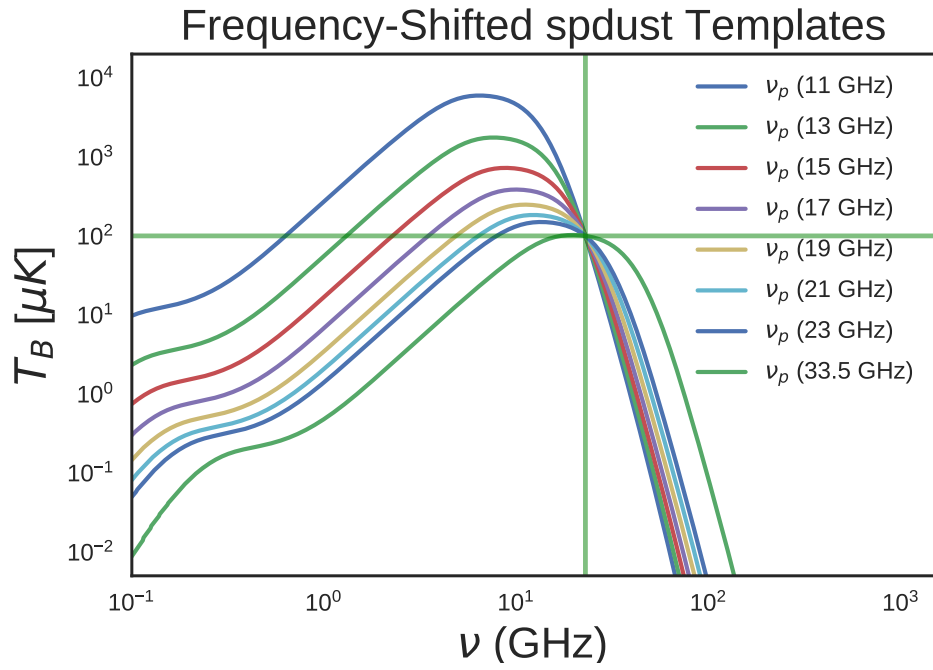


Figure 2.6: Spdust template spinning dust profiles fitted by PC15 when calculating AME_{var} . The reference frequency, 22.8 GHz is indicated by the vertical green line. Each template has the same AME_{var} amplitude of 100 μK , indicated by the horizontal green line, plotted to highlight the potential deviation between AME_{var} and the actual peak intensity.

all-sky survey tiles using the Aladin all-sky data visualization platform (Bonnarel et al. 2000). NSIDE 2048 implies an average pixel spacing of $1.7'$. The maps are then degraded to NSIDE 1024 before carrying out a Gaussian-beam smoothing to a 1° FWHM ⁷. Following the smoothing process, the maps are degraded once more to NSIDE 256, or 15arcmin pixel-width ⁸. The value of each of the larger NSIDE 256 pixels, comes from the mean of its parent NSIDE 1024 pixels. The purpose of this processing is to ensure that all of the maps have the same resolution as the PR2 AME map.

⁷To be clear, maps are converted first to spherical harmonic space, smoothed, and transformed back to position space using - steps carried about by the smoothing function contained in the healpy python package

⁸HEALPix pixel scale rebinning carried out with healpy.ud_grade

Chapter 3

All-sky Analysis

We first would like to note that “all-sky analysis” can be a bit misleading. The term tends to lead readers to the idea of a definitive study

We will first introduce our all-sky analysis of the AME vs. IR emission. This approach relies on HEALPix maps smoothed to 1° angular resolution. We start with an all-sky AME to IR comparison, looking for global patterns among all pixels (except those within 10° of the ecliptic plane.)

3.1 All-sky Pixel Domain Analysis

3.1.1 All-sky cross correlations

In order to look more closely how the the AME to IR relationship varies with wavelength, we first do a simple cross-correlation test. Figure ?? shows Spearman’s $\rho(r_S)$, for each of the 12 bands sampled.¹

¹Throughout this work we adopt r_s as our statistical metric. Rather than the linearity of potential IR-MW relationships, we are interested in the extent of monotonic relatedness.[sea](#)

3.1.2 Pixel mask

Zodical light To keep our analysis comparable to previous works, we exclude pixels within 10° of the ecliptic plane. Even though we use the Zodi-subtracted maps ((Kelsall et al. 1998; Kondo et al. 2016)), the Zodi residuals are still problematic (especially in the MIR.)²

3.1.3 AME data

The AME data comes from the PR2 astrophysical component datasets, as described in Ch. 2. We show the comparison for 3 different AME estimates: the two AME components (AME_{var} and AME_{fix}) as they are provided in PR2 (intensities quoted at reference frequencies³. The AME_{fix} peak freq. is spatially constant at 33.5 GHz), with AME_{var} and AME_{fix} calculated at each pixel's peak frequency rather than the PR2 reference freq. We do this because there is nothing physically special about the Planck reference frequencies, and because the PR2 AME_{var} component intensity could vary significantly from the intensity at the peak of the fitted spinning dust template. Thirdly we show the correlation matrix with a single AME metric- calculating the integrated intensity at each pixel, for both AME components, creating an AME_{sum} component.

Figure ?? visualizes the cross-correlation matrix for each of the IR bands. The AME does not show a strong correlation with other bands at $|l| > 10$. At $|l| < 10$, the FIR bands show stronger correlation. The PAH-tracing bands show a stronger correlation than bands at 18 to 60 μm , but weaker than AME vs. the FIR bands.

²Note that even at high ecliptic latitudes, the relative uncertainty of the Zodi-level is not well estimated; S/N may significantly reduced in for faint pixels, mainly for the 9 through 25 micron maps.

³22.8 GHz for AME_{var} , 41 GHz for AME_{fix}

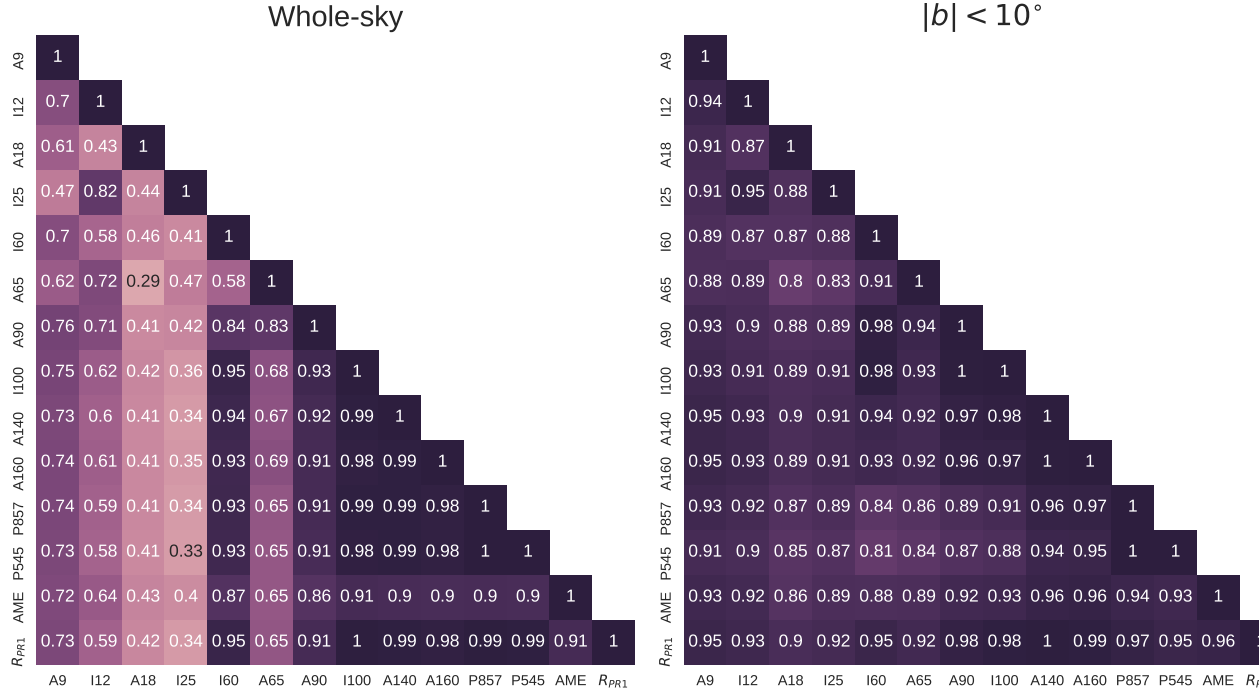


Figure 3.1: ALL-SKY cross-correlation matrix for the 18 infrared bands sampled, and the AME map. The color-scale indicates (r_s) . Results are based on the full sky (excluding pixels within 10° of the ecliptic plane).

3.2 Spatial variation of correlations

To understand how these trends may vary across the sky, we produce an all-sky maps of r_s for AME vs. IR emission. From the NSIDE 256 input maps of AME and 4 IR wavelength maps, we produce NSIDE 8 maps of r_s . These maps are shown in Fig. ??.

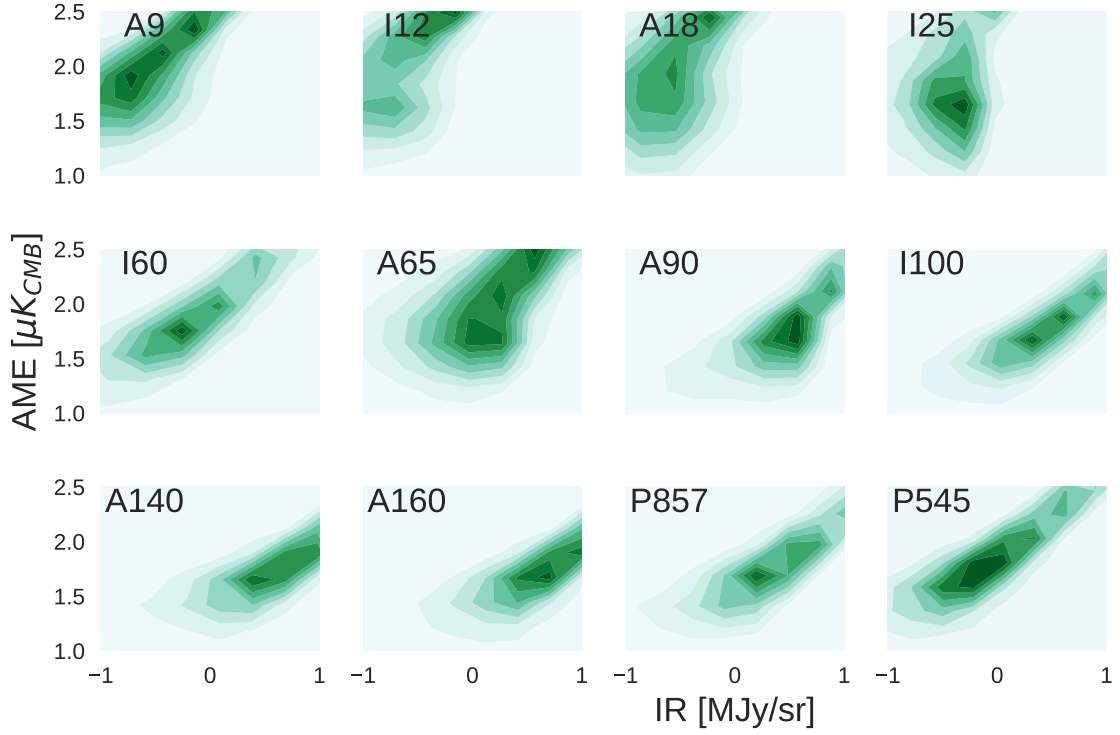


Figure 3.2: ALL-SKY kernel density estimates of 12-band infrared photometry against the PR2 AME map. Pixels within 10° of the ecliptic plane are excluded. 'A' indicates AKARI; 'D', DIRBE; 'I', IRAS, and 'P' Planck. The number after each letter indicates the band central nominal wavelength in microns (or frequency in GHz, in the case of the Planck bands.)

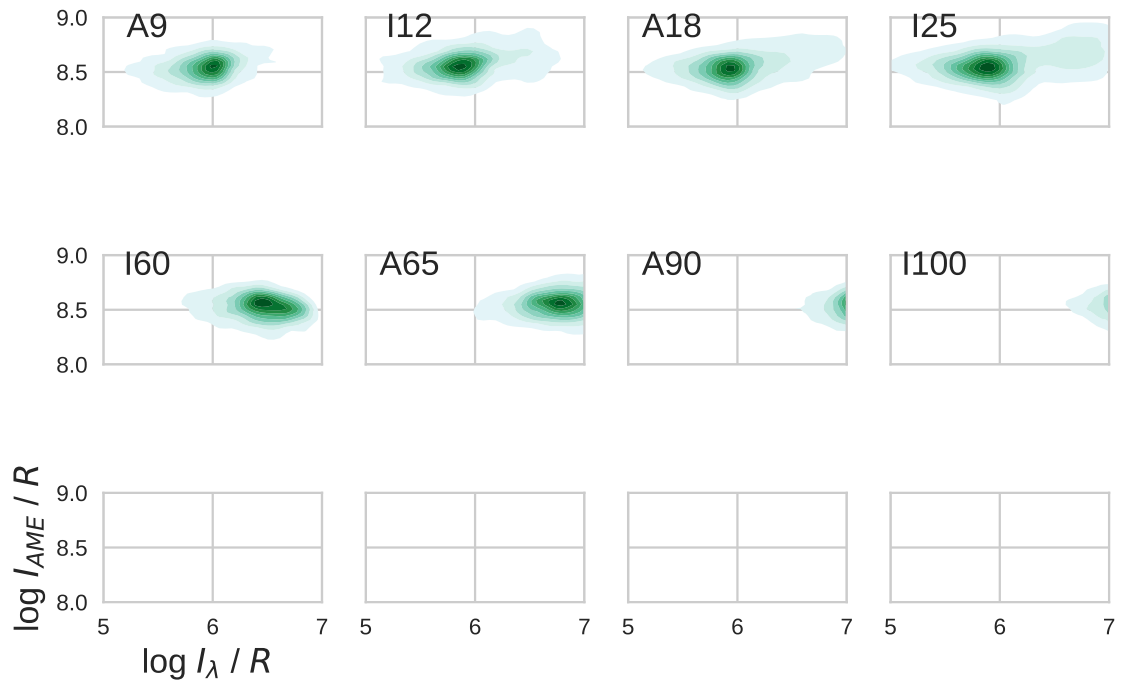
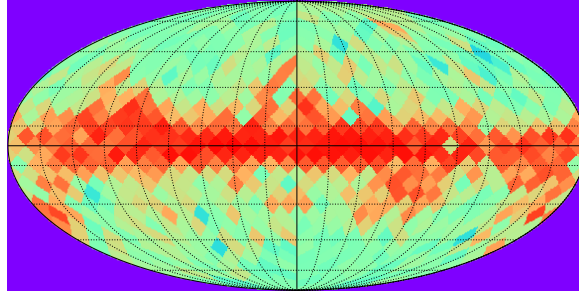
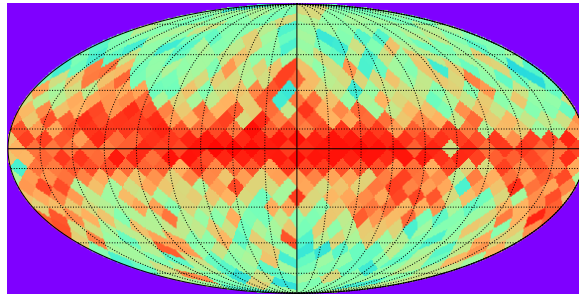


Figure 3.3: Similar comparison to Fig. ??, with both the IR and the AME intensities scaled by the PR2 dust radiance (R) for each pixel.

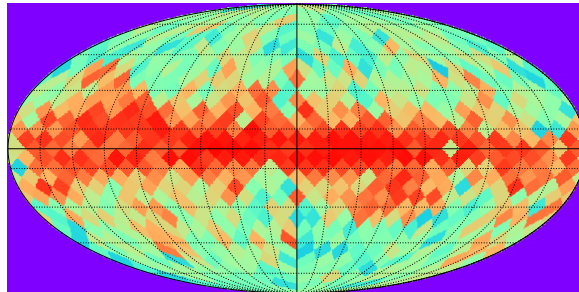
S(AME:A9) NSIDE



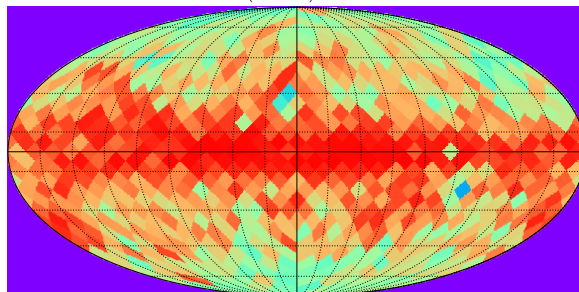
S(AME:i12) NSIDE



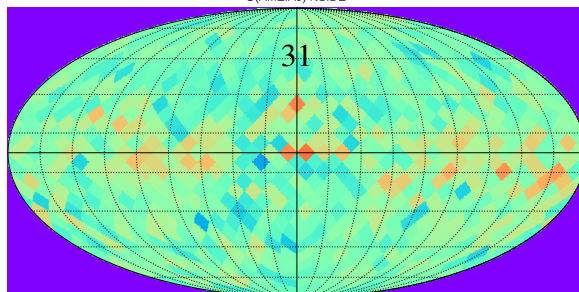
S(AME:i25) NSIDE



S(AME:A140) NSIDE



S(AME:A9) NSIDE



Chapter 4

Analysis of an interesting AME region: λ Orionis

4.1 An interesting AME region

The λ Orionis molecular ring ¹ is a massive stucture surrounding the λ Orionis O-type star. The ring contains an HII region, ionized by LOri itself and its OB associates (Murdin & Penston 1977). What had been thought of as a starforming region of missing molecular gas ²

Maddalena (1986); Maddalena & Morris (1987). (and references therein) noted a ring of material likely being pushed out by the central, historically well-known Lambda Orionis Association of B-type stars and surrounding HII reigon.

¹Also known as the Meissa Ring

²At the time Murdin & Penston (1977) even speculated that this could be evidence of an alternate starformation pathway, writing: “Notably we need to know if λ Ori is an example of a different mode of star formation or [...] simply a case in which the progenitor molecular cloud was exhausted within the last one or two million years.”

4.1.1 Where does the ring come from?

Cunha & Smith (1996) argued that the ring may have resulted from a supernova explosion, further speculating that LOri may have been a companion of the progenitor³. The central region is heated by the λ Orionis star itself, and the Orion OB association it belongs to (Ochsendorf et al. 2015). The region is known to host several young stellar and protostellar objects (Koenig et al. 2015).

At approx. 10° wide, we can see the outline of the structure even in the low (1° FWHM) resolution PCAME map. The ring shape itself is thought to originate from a supernova, or perhaps combined effects of the entire star formation history of the Lambda Orionis Association, including the formation of its surrounding HII region (ara ???).

4.1.2 A well-studied region

Although the LOri region has been a popular target for study since approximately 1982⁴, fewer works had looked into the ISM structure of the entire region. Many works have investigated the astrophysics of individual portions of this region. The large angular size is such that all-sky surveys were a natural boon for study of such extended structures. WISE especially was a huge source of insight (Koenig et al. 2015). More recently, the region was strongly highlighted by a Planck Collaboration microwave foregrounds follow-up investigation, as a strong candidate for further AME investigation (Planck Collaboration et al. 2016b).

³LOri is a known binary system, with its current companion being a B-type star. (Murdin & Penston 1977)

⁴Duerr et al. (1982) wrote of the relative lack of work on the overall region: “Surprisingly, this interesting complex has been little studied”

4.2 Investigative approach

We have carried out an initial comparison of the AME of this region with its mid to far-IR dust emission. The region is shown in Fig. ?? as it appears in 1°-smoothed A9 data⁵. The ring structure itself indicates excess microwave emission attributed to AME (white contours) while the central region is dominated by free-free emission (ara ???; Koenig et al. 2015; Planck Collaboration et al. 2016b). Taking the hint from Planck Collaboration et al. (2016b) that this may be among the more reliably component separated regions appearing in the PCAME map, we evaluate if there is any preferential relationship between any parameter of dust emission and the AME.

4.2.1 Data preparation

As indicated in Ch. 2, we use 12 photometric all-sky maps. For the IRC data (A9 and A18), we produce mosaics of LOr from the individual tiles provided in the internal all-sky archive.⁶ For the other sources, HEALPix all-sky maps are available publicly, at sufficient resolution relative to their native resolutions.⁷⁸⁹

⁵Images at each wavelength used here are included as in appendix to this thesis

⁶IRC all-sky data is still in the proprietary phase at the time of this writing, but should be public by April 2018.

⁷Planck data was retrieved from the NASA IPAC online archive at http://irsa.ipac.caltech.edu/data/Planck/release_2/all-sky-maps/

⁸AKARI/FIS data

⁹IRAS/IRIS data

4.2.2 Extraction from HEALPix maps

For the data obtained via HEALPix maps, we employ the “healpix2wcs” functionality provided in the “gnomdrizz” python package¹⁰¹¹ A9 and A18 images are produced by regridding the images with the “montage” software by NASA/IPAC. All of the images for all of the bands are based on a common FITS header which has a pixel grid spacing equal to the average pixel width in the NSIDE 256 HEALPix scheme. A background estimation and subtraction is made

4.2.3 Multi-wavelength characterization

Figure ?? shows the region in 12 photometric bands, from the mid to far IR. Contours indicate the region’s shape in the PCAME map. Figure ?? shows IR to AME cross correlation plots, for all pixels within the 10° by 10° λ Orionis region. The correlation is most clear for the shortest and for the longest wavelength bands, and weakens the most at around $60 \mu\text{m}$. The weakening of the correlation score appears to come from brighter 25 to $90 \mu\text{m}$ emission within the ring. The spectrum is consistent with warm thermal dust emission, heated by λ Orionis and its associates. The ring structure itself appears relatively consistent accross all bands. Fig.

4.2.4 Ionization fraction

We attempt to estimate the relative fraction of charged to neutral PAHs via the R(A9:I12) band ratio. A9 is known to cover ionized PAH features (as well as

¹⁰Available at <http://cade.irap.omp.eu/dokuwiki/doku.php?id=software>

¹¹“drizzlib” 1.2.2 and earlier were not able to correctly access HEALPix files with multiple fields/columns. See appendix for our recommended workaround.

neutral) whereas I12 primarily covers neutral features.

4.2.5 SED Fitting

We performed a full dust SED fitting on the LOri photometry, according to the Galliano et al. (2011) dust model. We used a mixture of amorphous carbon and silicate dust. Indeed, this dust mixture is more emissive than the standard silicate-graphite (Draine & Li 2007), by a factor of 2-3. As was shown by Herschel, in the LMC (Galliano et al. 2011), and by Planck, in the Milky Way (Planck Collaboration et al. 2016c), this increase of emissivity is necessary to have a proper fit of the sub-mm emission. We assume that the radiation field heating this dust mixture is the Galactic ISRF (Mathis et al. 1983), scaled by a factor U . We also assume, following Dale et al. (2001), that the dust is exposed to a distribution of starlight intensity, distributed as:

$$dM_{dust} \propto U^{-\alpha} dU \quad (4.1)$$

between U_{min} and U_{max} , where U_{min} , U_{max} and α are free parameters. An old stellar population template (PEGASE; (Fioc & Rocca-Volmerange 1997)) is added to this SED in order to model the near-IR emission. We perform a simple least-squares analysis.

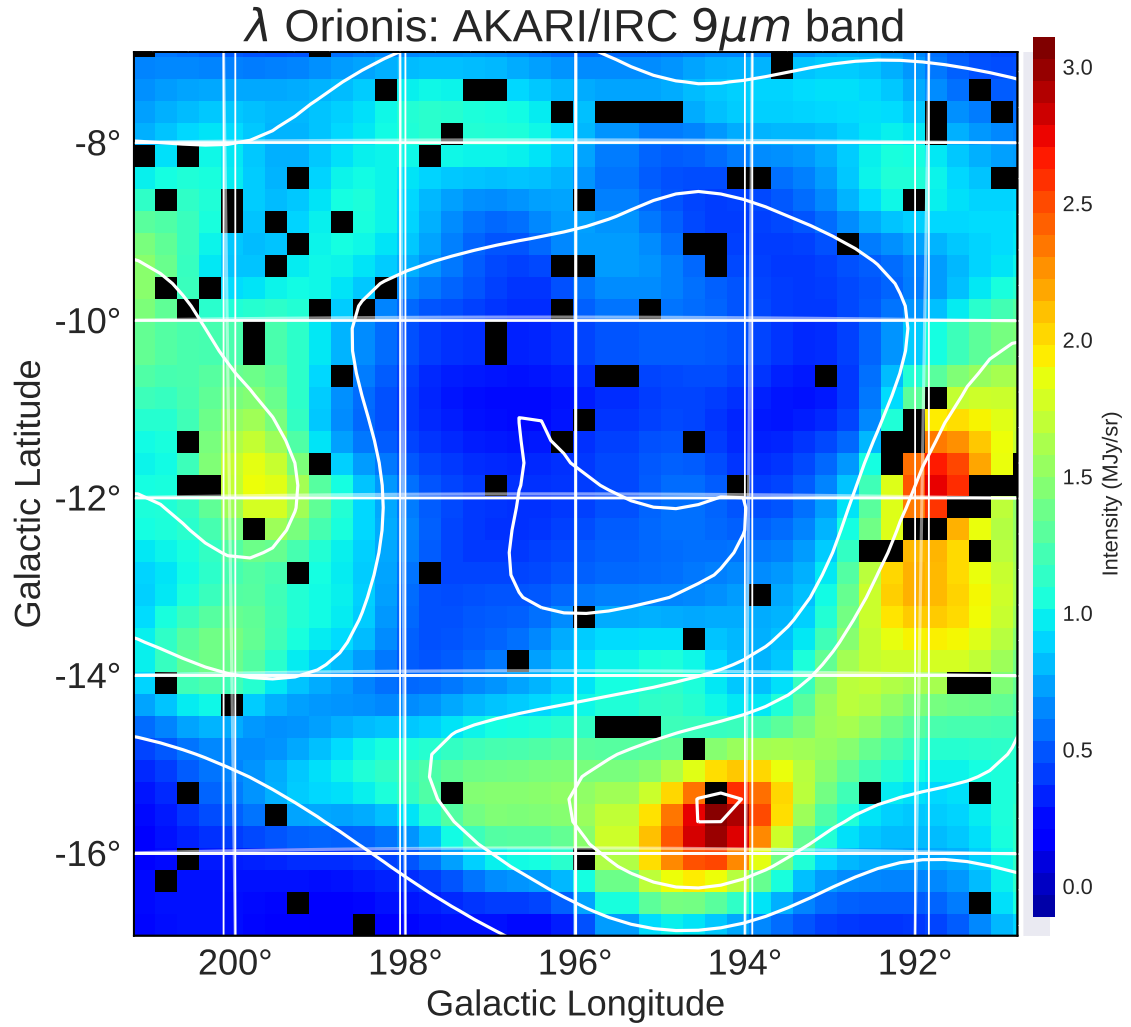


Figure 4.1: λ Orionis as it appears in the AKARI 9 μ m data. Contours indicate the AME, as given by the Planck PR2 AME map. The image is smoothed to a 1° PSF (much larger than the original 10 arcsec map). The λ Orionis star itself is approximately located at the center of the image.

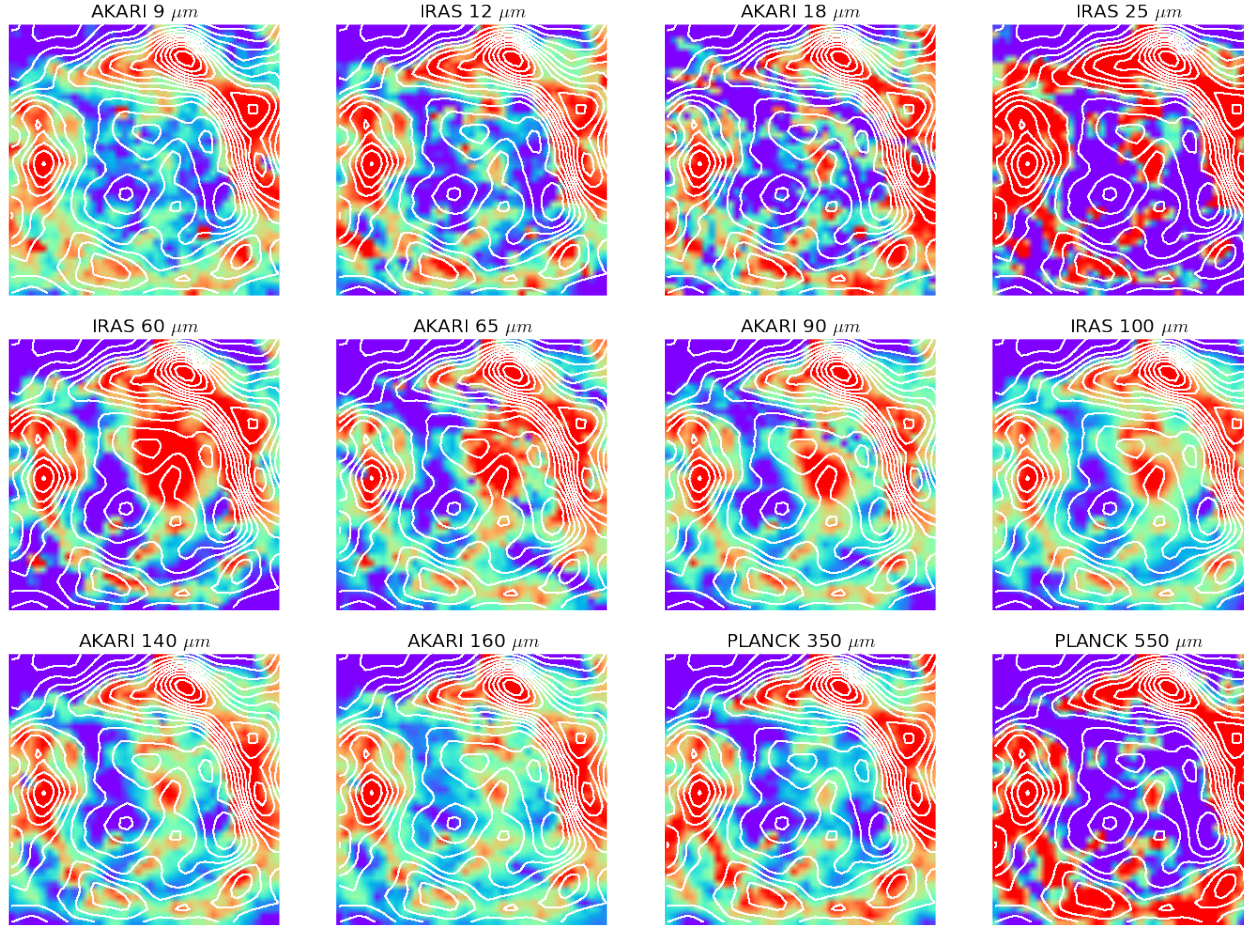


Figure 4.2: A grid of thumbnails showing the λ Orionis region's structure, at 12 wavelengths, along with AME contours (shown in white contours). Spatial correlation seems to be the best at the shortest and longest wavelengths (AKARI/IRC 9 μm and Planck/HFI 550 μm). The images are smoothed and interpolated for demonstration. Figure ?? demonstrates the actual pixel grid used for the SED fitting and intensity correlation tests.

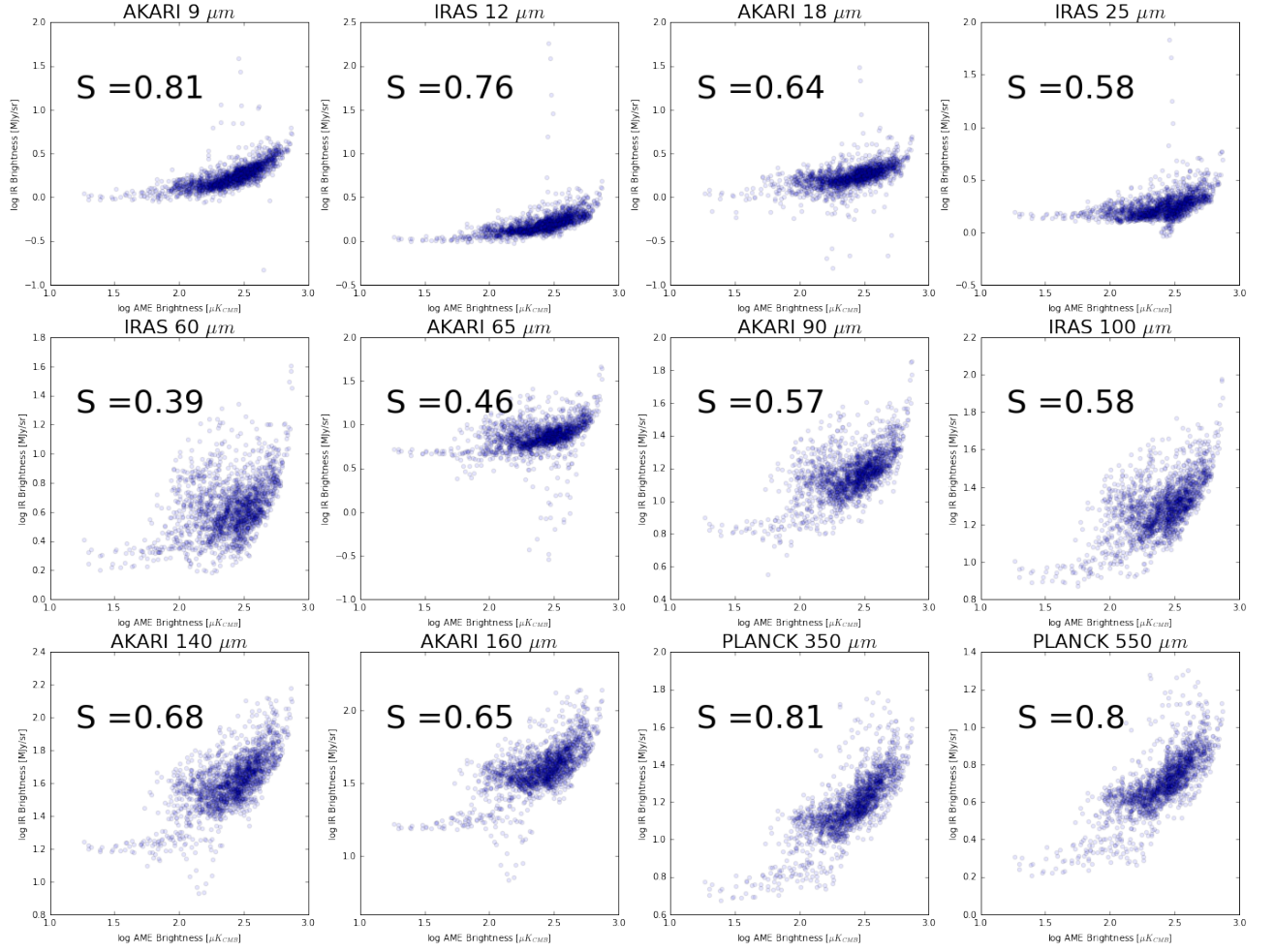


Figure 4.3: Pixel cross-correlation for all pixels in the λ Orionis cut-out region. r_s indicates the Spearman rank correlation coefficient for each plot.

Chapter 5

Discussion

We have compared AME with infrared dust emission from 2 approaches. The results and discussion contained here apply to an angular scale of approximately 1° . In general, our results support an AME-from-dust hypothesis. At 1° angular resolution, we do not find evidence that the AME is exclusively carried by PAHs. The correlation of far IR dust emission with AME appears to be the best predictor, with MIR/PAH emission being marginally more weakly correlated with AME. As far as the MIR bands are concerned, at least in terms of intensity, $I_{9\mu m}$ shows the strongest correlation. This result is mirrored in LOri, however in that case $I_{9\mu m}$ and $I_{545\mu m}$ show the strongest correlation. In the case of λ Orionis, AME vs. PAH emission is at least as strong as AME vs. FIR emission.

5.1 AME:Dust

As noted in Ch. 1, previous studies found that the AME generally correlates at dust-related IR wavelengths (Ysard et al. 2010; Planck Collaboration et al. 2014c;

Hensley et al. 2016). We see the same overall pattern in the present study, for both the all-sky pixel-based analysis, and the inspection of the λ Orionis region.

In our all-sky comparison, we find a first-order correlation between IR intensity and AME intensity, for each of the 12 wavelengths sampled. This is again consistent with the previous investigations of the AME cited above, in that the FIR emission shows the tightest correlation with the AME intensity.

In testing for a second-order correlation, we divided the IR intensities and AME intensity by the dust radiance, and again performed the band-by-band all-sky comparison. There is evidence of a residual correlation between I_{MIR} and I_{AME}/R . Unsurprisingly, the strong correlation between I_{FIR} and I_{AME} disappears when scaling by R , as the the FIR bands are dominated by thermal dust emission. In this case, we again find no evidence of an improved correlation for the PAH-dominated bands.

The closeness of the correlation coefficients found here is consistent with the results of the IRAS vs. AME correlation test result from Planck Collaboration et al. (2014c). They found that the correlation coefficient among the 4 IRAS bands (12, 25, 60, and 100 μm) differ from one another only by about 5%, across the whole set of 98 regions. The trend of AKARI MIR and FIR data vs. the AME does not disagree with their IRAS comparison. This work adds that bands longer than IRAS 100 μm also correlate strongly with AME, especially the two Planck/HFI bands used.

5.2 AME:PAH

In the case of λ Orionis we found that accross the whole region, AKARI 9 μm emission and Planck 545 GHz emission were the most strongly correlated with AME, having Spearman coefficients of 0.81 and 0.80. The results may be consistent with a scenario in which PAH mass, cold dust, and the AME are all tightly correlated. Weaker correlation from 25 to 70 μm may indicate that AME is weaker in regions of warmer dust and stronger radiation fields. This would be consistent with PCXV wherein highly significant AME regions tended to have a lower dust temperature than other regions. The fact that the correlation strengths of PAH-tracing mission the FIR emission are similar is in-line with what we have seen in Ysard et al. (2010) and Hensley et al. (2016). In those works, the two relationships (MIR vs. AME and FIR vs. AME) are very close, although these two papers are odds as to which relationship is stronger, and thus in their final interpretation. However in the investigation of the Perseus molecular cloud complex by Tibbs et al. (2011), PAH emission (as well as VSG emission and hydrogen column density, N_H) does not show a strong correlation with AME compared to environmental paramters, such as dust temperature.

On an all-sky basis, each of the bands sampled show correlation with the AME, however the FIR bands always show the strongest correlation. In fact, the correlation pattern of AME vs. each of the IR bands, very strongly resembles the correlation results of the Planck HFI bands vs. all of the other bands (Fig. ??.) This is readily apparent from the pixel-density plots in Fig. ??, wherein the FIR bands pixels show a very similar density profile vs. the AME. In attempting to factor out this first-order correlation, dividing the AME and IR intensities by

the dust radiance for each pixel, we find there is still a residual correlation between the MIR bands and the AME. The FIR bands scaled by the dust radiance, as expected, lack correlation with I_{AME}/R .

5.3 AME: T , G_0

According to spinning dust theory outlined in Draine & Lazarian (1998a) and in subsequent works by Ysard & Verstraete (2010), the AME profile and intensity will depend in part on the ISRF- but as is well-stated in Hensley & Draine (2017a), exactly how the ISRF will affect the AME SED is a more complicated question. Absorbed starlight photons may be able to rotationally excite the carriers, but if an enhanced ISRF leads to increased dust heating, then the increased IR emission can rotationally de-excite the carriers. However the ISRF affects not only the dust temperature but ionization of the carriers.

Hensley et al. (2016) looked at the AME/R ratio vs. T and found only a slight anti-correlation of $P = -0.06$.

5.4 Microwave foreground component separation

There are known degeneracies between the foreground parameters of the COMMANDER maps (spinning-dust, and free-free, synchrotron components as described in Planck Collaboration et al. (2016a).) This can be demonstrated by comparing the ratio map of the PCXV intensity to thermal dust intensity.

Chapter 6

Summary

From these results, we cannot confirm or rule out a spinning-PAH hypothesis on an all-sky, 1° scale. While nanosilicates or magnetic dipole emission from dust may be plausible contributors to the AME, as shown in Hoang et al. (2016); Hensley & Draine (2017a), we do not find (at least at resolutions considered here) that PAHs can be ruled-out as a carrier. While it is true that the FIR in our study has a tighter correlation with AME than PAH-related bands, the correlation with PAH emission remains. This is true both when considering AME intensity to Either this is a coincidental correlation- PAHs and AME are both correlated with the “actual” carrier/s of AME, MIR photometric bands are not as good of a tracer of the actual PAH mass as we believed, or perhaps that PAHs are indeed contributing to the AME but that they are just one of multiple sources of the AME.

If it can be shown that IR emission from non-PAH small dust particles, such as nanosilicates strongly correlates with the AME, another very interesting question would need to be addressed: why does PAH emission *not* show a strong correlation? Do PAHs not have the range of dipole moments needed to produce emission

in the 10 - 90 GHz range? Because, as is described in Draine & Lazarian (1998a) and again in Hensley & Draine (2017b), such small particles should be spinning at the frequencies consistent with AME. Thus if we believe a particular class of small dust particles to exist, PAHs, nanosilicates, or otherwise- then they must be producing microwave emission, unless they do not have a permanent electric dipole.

If there is a sufficient abundance of PAHs with an electric dipole, then we must consider the possibility that the data currently available to do not offer the necessary spatial resolution, or that the photometric bands used do not allow us to adequately separate the individual dust components (i.e. the PAH features from potential nanosilicate features) and/or microwave foreground emission components (free-free from spinning-dust.) We look forward to continued environment-resolved comparisons to investigate the potential AME-PAH (or AME-nanosilicates, iron nanoparticles) relationship in a region by region, especially given the disagreement we find between our examination of λ Orionis and the all-sky analysis.

This project is supported by JSPS and CNRS under the Japan–France Research Cooperative Program. We would like to give special thanks to the AME Workshop 2016 attendees and organizer, Chris Tibbs, for enlightening discussions. Thanks also to Nathalie Ysard and Steven Gibson, and the staff of Grid, Inc. for helpful feedback.

A Note on Data Dimensionality

While we aim to demonstrate the application of high dimensionality in these studies, we do not wish to mislead readers that we have assembled a 12-dimensional photometric dataset, simply because we have 12 wavebands. This statement may seem nonsensical at first, but makes sense when we consider the covariance of the data. Just from the outside, and our faithful belief that FIR dust emission looks something like a blackbody, or modified blackbody, or at the very least we can agree that emission from dust in thermal equilibrium would produce some sort of peaked continuum emission spanning multiple photometric bands' width. If we agree on this point, then it follows naturally that said bands would be highly correlated with one another. This means that the number of truly independent data dimensions is not only lower than the number of bands used here, it is much lower.

Fig. ?? shows the % of variance in the data retained by the first n principal components. Principal components are found essentially by first finding the covariance matrix of the input data, and then diagonalizing this matrix- the eigenvectors will be the basis vectors of each principal component. The eigenvalues will give the explained covariance per component. Applied in this manner, the components may not necessarily have a clear physical interpretation, but from a data analytics perspective we can at least assess the redundancies in our data. Thus

from Fig. ??, and choosing an arbitrary covariance “acceptable loss” of 99%, our photometric data set steeply reduces to 3 dimensions. The first component contains 98% of the total variance.

How many useful components are in our data?

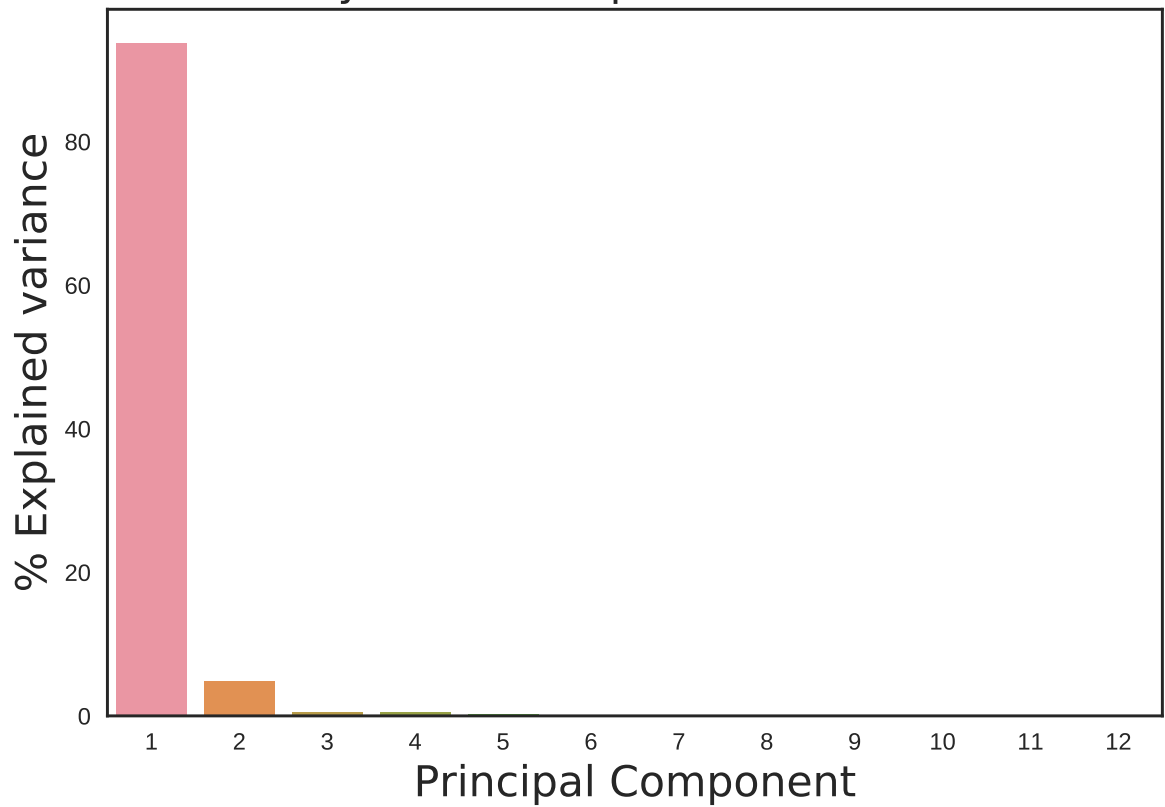


Figure 1: Explained variance decline for principal component analysis performed on a set of 12 all-sky infrared maps. The first three components account for over 99% of the total variance. The PCA fit is performed on the whole sky, after whitening the data, using the “scikitlearn

This research made use of Montage. It is funded by the National Science Foundation under Grant Number ACI-1440620, and was previously funded by the National Aeronautics and Space Administration's Earth Science Technology Office, Computation Technologies Project, under Cooperative Agreement Number NCC5-626 between NASA and the California Institute of Technology

Bibliography

????, PhD thesis

Ali-Haïmoud, Y. 2010, SpDust/SpDust.2: Code to Calculate Spinning Dust Spectra, Astrophysics Source Code Library

Ali-Haïmoud, Y. 2014, MNRAS, 437, 2728

Ali-Haïmoud, Y., Hirata, C. M., & Dickinson, C. 2009, MNRAS, 395, 1055

AMI Consortium et al. 2012, MNRAS, 423, 1463

Andrews, H., Boersma, C., Werner, M. W., Livingston, J., Allamandola, L. J., & Tielens, A. G. G. M. 2015, ApJ, 807, 99

BICEP2 Collaboration et al. 2014, Physical Review Letters, 112, 241101

Bonnarel, F., et al. 2000, A&AS, 143, 33

Compiègne, M., et al. 2011, A&A, 525, A103

Cunha, K., & Smith, V. V. 1996, A&A, 309, 892

Dale, D. A., Helou, G., Contursi, A., Silberman, N. A., & Kolhatkar, S. 2001, ApJ, 549, 215

- de Oliveira-Costa, A., Kogut, A., Devlin, M. J., Netterfield, C. B., Page, L. A., & Wollack, E. J. 1997, *ApJ*, 482, L17
- Dickinson, C., Paladini, R., & Verstraete, L. 2013, *Advances in Astronomy*, 2013, 1
- Doi, Y., et al. 2015, *PASJ*, 67, 50
- Draine, B. T. 2011, *Physics of the Interstellar and Intergalactic Medium*
- Draine, B. T., & Hensley, B. 2013, *ApJ*, 765, 159
- Draine, B. T., & Lazarian, A. 1998a, *ApJ*, 494, L19
- . 1998b, *ApJ*, 508, 157
- . 1999, *ApJ*, 512, 740
- Draine, B. T., & Li, A. 2007, *ApJ*, 657, 810
- Duerr, R., Imhoff, C. L., & Lada, C. J. 1982, *ApJ*, 261, 135
- Erickson, W. C. 1957, *ApJ*, 126, 480
- Ferrara, A., & Dettmar, R.-J. 1994, *ApJ*, 427, 155
- Fioc, M., & Rocca-Volmerange, B. 1997, *A&A*, 326, 950
- Flauger, R., Hill, J. C., & Spergel, D. N. 2014, *J. Cosmology Astropart. Phys.*, 8, 039
- Galliano, F., et al. 2011, *A&A*, 536, A88
- Giard, M., Lamarre, J. M., Pajot, F., & Serra, G. 1994, *A&A*, 286
- Górski, K. M., Hivon, E., Banday, A. J., Wandelt, B. D., Hansen, F. K., Reinecke, M., & Bartelmann, M. 2005, *ApJ*, 622, 759

- Hanson, D., et al. 2013, *Physical Review Letters*, 111, 141301
- Haslam, C. G. T., Salter, C. J., Stoffel, H., & Wilson, W. E. 1982, *A&AS*, 47, 1
- Hensley, B. S., & Draine, B. T. 2017a, *ApJ*, 836, 179
- . 2017b, *ApJ*, 834, 134
- Hensley, B. S., Draine, B. T., & Meisner, A. M. 2016, *The Astrophysical Journal*, 827, 45
- Hoang, T., Draine, B. T., & Lazarian, A. 2010, *ApJ*, 715, 1462
- Hoang, T., Vinh, N.-A., & Quynh Lan, N. 2016, *ApJ*, 824, 18
- Hoyle, F., & Wickramasinghe, N. C. 1970, *Nature*, 227, 473
- Ishihara, D., et al. 2010, *A&A*, 514, A1
- Johnson, H. L. 1966, *ARA&A*, 4, 193
- Jones, A. P. 2009, *A&A*, 506, 797
- Kawada, M., et al. 2007a, *PASJ*, 59, 389
- . 2007b, *PASJ*, 59, S389
- Kelsall, T., et al. 1998, *ApJ*, 508, 44
- Koenig, X., Hillenbrand, L. A., Padgett, D. L., & DeFelippis, D. 2015, *AJ*, 150, 100
- Kogut, A., Banday, A. J., Bennett, C. L., Gorski, K. M., Hinshaw, G., & Reach, W. T. 1996, *ApJ*, 460, 1
- Kondo, T., et al. 2016, *AJ*, 151, 71
- Leitch, E. M. 1998, PhD thesis, CALIFORNIA INSTITUTE OF TECHNOLOGY

- Li, A., & Draine, B. T. 2001, *ApJ*, 554, 778
- Lovas, F. J., McMahon, R. J., Grabow, J.-U., Schnell, M., Mack, J., Scott, L. T., & Kuczkowski, R. L. 2005, *Journal of the American Chemical Society*, 127, 4345, PMID: 15783216
- Maddalena, R. J. 1986, PhD thesis, National Aeronautics and Space Administration. Goddard Inst. for Space Studies, New York, NY.
- Maddalena, R. J., & Morris, M. 1987, *ApJ*, 323, 179
- Mathis, J. S., Mezger, P. G., & Panagia, N. 1983, *A&A*, 128, 212
- Miville-Deschênes, M.-A., & Lagache, G. 2005, *ApJS*, 157, 302
- Murakami, H., et al. 2007, *PASJ*, 59, 369
- Murdin, P., & Penston, M. V. 1977, *MNRAS*, 181, 657
- Neugebauer, G., et al. 1984, *ApJ*, 278, L1
- Ochsendorf, B. B., Brown, A. G. A., Bally, J., & Tielens, A. G. G. M. 2015, *ApJ*, 808, 111
- Onaka, T. 2000, *Advances in Space Research*, 25, 2167
- Onaka, T., Yamamura, I., Tanabe, T., Roellig, T. L., & Yuen, L. 1996, *PASJ*, 48, L59
- Onaka, T., et al. 2007, *PASJ*, 59, 401
- Penzias, A. A., & Wilson, R. W. 1965, *ApJ*, 142, 419
- Perrott, Y. C., et al. 2018, *MNRAS*, 473, 1157
- Planck Collaboration et al. 2014a, *A&A*, 571, A8

—. 2014b, A&A, 571, A12

—. 2014c, A&A, 565, A103

—. 2016a, A&A, 594, A10

—. 2016b, A&A, 594, A25

—. 2016c, A&A, 586, A132

Reynolds, R. J., Tufte, S. L., Haffner, L. M., Jaehnig, K., & Percival, J. W. 1998, PASA, 15, 14

Takita, S., et al. 2015, PASJ, 67, 51

Thorwirth, S., Theulé, P., Gottlieb, C. A., McCarthy, M. C., & Thaddeus, P. 2007, ApJ, 662, 1309

Tibbs, C. T., et al. 2011, MNRAS, 418, 1889

Ysard, N., Juvela, M., & Verstraete, L. 2011, A&A, 535, A89

Ysard, N., Miville-Deschênes, M. A., & Verstraete, L. 2010, A&A, 509, L1

Ysard, N., & Verstraete, L. 2010, A&A, 509, A12